applied sciences

MDPI

Article

Towards Patient Anatomy-Based Simulation of Net Cerebrospinal Fluid Flow in the Intracranial Compartment

Edgaras Misiulis [1,2,*], Algis Džiugys [2], Alina Barkauskienė [3], Aidanas Preikšaitis [4,5], Vytenis Ratkūnas [6], Gediminas Skarbalius [2], Robertas Navakas [2], Tomas Iešmantas [1], Robertas Alzbutas [1,7], Saulius Lukoševičius [8], Mindaugas Šerpytis [5,9], Indrė Lapinskienė [5,9], Jewel Sengupta [1] and Vytautas Petkus [6]

1 Faculty of Mathematics and Natural Sciences, Kaunas University of Technology, K. Donelaičio g. 73, LT-44249 Kaunas, Lithuania; tomas.iesmantas@ktu.lt (T.I.); robertas.alzbutas@ktu.lt (R.A.); jewel.sengupta@ktu.lt (J.S.)
2 Laboratory of Heat-Equipment Research and Testing, Lithuanian Energy Institute, Breslaujos g. 3, LT-44403 Kaunas, Lithuania; algis.dziugys@lei.lt (A.D.); gediminas.skarbalius@lei.lt (G.S.); robertas.navakas@lei.lt (R.N.)
3 Center of Radiology and Nuclear Medicine, Vilnius University Hospital Santaros Klinikos, Santariškių g. 2, LT-08661 Vilnius, Lithuania; alina.barkauskiene@santa.lt
4 Clinic of Neurology and Neurosurgery, Institute of Clinical Medicine, Faculty of Medicine, Vilnius University, M. K. Čiurlionio g. 21, LT-03101 Vilnius, Lithuania; danas911@gmail.com
5 Vilnius University Hospital Santaros Klinikos, Santariškių g. 2, LT-08661 Vilnius, Lithuania; mindaugas.serpytis@santa.lt (M.Š.); lapinskiene.indre@gmail.com (I.L.)
6 Health Telematics Science Institute, Kaunas University of Technology, K. Donelaičio g. 73, LT-44249 Kaunas, Lithuania; vytenisra@gmail.com (V.R.); vytautas.petkus@ktu.lt (V.P.)
7 Laboratory of Nuclear Installation Safety, Lithuanian Energy Institute, Breslaujos g. 3, LT-44403 Kaunas, Lithuania
8 Department of Radiology, Faculty of Medicine, Medical Academy, Lithuanian University of Health Sciences, A. Mickevičiaus g. 9, LT-44307 Kaunas, Lithuania; saulius.lukosevicius@lsmu.lt
9 Clinic of Anaesthesiology and Intensive Care, Institute of Clinical Medicine, Faculty of Medicine, Vilnius University, M. K. Čiurlionio g. 21, LT-03101 Vilnius, Lithuania
* Correspondence: edgaras.misiulis@lei.lt

Featured Application

The proposed patient anatomy-based cerebrospinal fluid flow simulation framework predicts steady net intracranial flow pathways and may support future clinical translation in conditions such as subarachnoid hemorrhage, hydrocephalus, and brain tumors.

Abstract

Biophysics-based, patient-specific modeling remains challenging for clinical translation, particularly for cerebrospinal fluid (CSF) flow where anatomical detail and computational cost are tightly coupled. We present a computational framework for steady net CSF redistribution in an MRI-derived cranial CSF domain reconstructed from T_2-weighted imaging, including the ventricular system, cranial subarachnoid space, and periarterial pathways, to the extent resolvable by clinical MRI. Cranial CSF spaces were segmented in 3D Slicer and a steady Darcy formulation with prescribed CSF production/absorption was solved in COMSOL Multiphysics®. Geometrical and flow descriptors were quantified using region-based projection operations. We assessed discretization cost–accuracy trade-offs by comparing first- and second-order finite elements. First-order elements produced a 1.4% difference in transmantle pressure and a <10% difference in element-wise mass-weighted velocity metric for 90% of elements, while reducing computation time by 75% (20 to 5 min) and peak memory usage five-fold (150 to 30 GB). This proof-of-concept framework provides a computationally tractable baseline for studying steady net CSF pathway redistribution and sensitivity to boundary assumptions, and may support future

Academic Editor: Mauro Malvè

Received: 11 November 2025
Revised: 20 December 2025
Accepted: 30 December 2025
Published: 7 January 2026

patient-specific investigations in pathological conditions such as subarachnoid hemorrhage, hydrocephalus and brain tumors.

Keywords: finite element method; computational fluid dynamics; cerebrospinal fluid; subarachnoid space; patient-specificity; periarterial space

1. Introduction

Computational fluid dynamics (CFD) and related numerical methods have become valuable tools for testing hypotheses on cerebrospinal fluid (CSF) transport and redistribution. Recent studies have investigated potential driving mechanisms of CSF motion in perivascular space [1–6], mechanisms that may affect blood clearance from the CSF after subarachnoid hemorrhage (SAH) [7–9], patient-specific CSF dynamics [10], and intrathecal drug delivery along CSF pathways [11]. Importantly, computational models enable the estimation of quantities that are difficult to measure in vivo, such as the transmantle pressure gradient [12].

The CFD applications extend from modeling specific isolated anatomical structures, such as a single ventricle or spinal canal, to encompassing the entire subarachnoid space (SAS) region, including the cerebral ventricular system (CVS). In addition, some of these studies also incorporated time-dependent CSF flow disturbances due to breathing, cardio cycles, etc.

Recent studies on patient-specific CSF dynamics integrate medical imaging data from MRI or CT, and transition from rigid-wall models towards fluid–structure interaction (FSI) models. These efforts aim to predict physiological and pathological flow patterns between individual patients and to support diagnosis and surgical planning. The CFD frameworks for the entire brain were developed based on a patient-specific 3D geometry of the CSF-filled spaces segmented from MRI, which also included various CSF pulsation drivers, such as cardiac cycle and coughing [13,14]. The existing barriers and pathways to clinically useful CFD simulation were discussed in [15]. However, to our knowledge, all current attempts have been limited by over-smoothing or using uniform cranial SAS thickness [10].

Based on these studies, it can be concluded that numerical modeling of the entire SAS region demands significant computational resources and time, especially for time-dependent analyses, which further increase these costs. Usually, a compromise must be made between computational costs and the complexity of both SAS and time-dependent phenomena.

A significant hurdle for the simulations is the sheer complexity of the SAS shape and its internal structures [16]. Patient-specific SAS representation (limited by today's imaging resolution) comprises more than ten million voxels. The spatial scale of internal SAS structures is much smaller than the scale of the whole brain. For example, the SAS contains many sulci, which are relatively long, narrow recesses extending toward the parenchyma, and the SAS also includes thin structures that envelop the cerebrovascular system (perivascular spaces) [17].

Until now, the computational complexity was reduced by coarsening and smoothing out SAS, and as a result, losing spatial information of any thin structures such as sulci or major perivascular spaces [7]. Under high-pressure conditions, such as the influx of blood into the subarachnoid space following an aneurysmal subarachnoid hemorrhage (aSAH), sulci and perivascular spaces may play a critical role in determining patient outcomes and should therefore be incorporated into CSF flow models. The importance of including perivascular spaces and sulci in the CSF flow model for aSAH patients is

evident, as CT scan data of aSAH patients show that a significant portion of blood ends up in the perivascular (vessel-adjacent) regions [18]. The importance of patient-specific SAS cross-sectional areas could be manifested in aSAH patients. It was demonstrated that younger aSAH patients tend to develop vasospasms more often compared to older aSAH patients [19]. Apart from other mechanisms, such as higher vessel elasticity, this could also be attributed to the smaller cross-sectional areas of SAS, as with age, the cross-sectional area of SAS increases [17].

Therefore, in this paper, we present a pilot finite element method (FEM)-based model of CSF flow that incorporates a patient-specific 3D representation of the cranial CSF space (cCSFS), comprising the cerebral ventricular system, CVS, cranial subarachnoid space (cSAS), and periarterial space (PVS), to the extent resolved by MRI acquisition. The segmentation was manually corrected to remove non-anatomical connections while preserving MRI-resolved morphology and connectivity. We additionally evaluate the computational trade-off between first- and second-order finite elements (details in the Materials and Methods Section). To the best of our knowledge, this work represents one of the most geometrically detailed patient-specific reconstructions used for whole-domain CSF redistribution modeling to date, and it demonstrates the feasibility of MRI-level geometric fidelity within a tractable numerical framework. Although the ventricular system is not porous in vivo, we employ a Darcy formulation over the full cCSFS as an effective model for net flow distribution; this choice also maintains consistency with extensions that represent obstructing material (e.g., clots) as porous regions, while explicit hemorrhage simulations are outside the scope of the present study.

2. Materials and Methods

Approval of all experimental procedures and protocols was granted by Vilnius Regional Biomedical Research Ethics Committees (Protocol No. 2021/9-1370-847) and performed in line with the 1964 Declaration of Helsinki and its subsequent revision (up to October 2024).

2.1. Subject Selection

A single, healthy, 42-year-old male subject from Vilnius University Hospital Santaros Clinics was enrolled for this study. The subject had no previous history of neurological or cardiovascular disorders.

2.2. MRI Scan Protocol

The subject's brain was scanned with a Philips Achieva 3 T MR scanner (Philips Healthcare, Best, The Netherlands). During the scanning, the subject was lying supine with his neck in a neutral position. To maximize the contrast of the intracranial CSF, the MRI was obtained by performing the sequence of T_2-weighted Drive HR with the following parameters: TE 226 ms, TR 1.6 ms, FA 90, section thickness 1.3 mm, and voxel size $0.59 \times 0.50 \times 1.3$ mm.

2.3. Segmentation

The 3D Slicer v5.1 software [20,21] was used for cCSFS volume segmentation, visual inspection, and correction, while the COMSOL Multiphysics® v6.0 [22] was used for CSF flow pattern prediction and visual inspection to identify intricate non-anatomical cCSFS connections. We define cCSFS as a space composed of the cranial subarachnoid space, periarterial space, and ventricular system reconstructed up to MRI resolution.

The final cCSFS segmentation was obtained in several steps. The initial segmentation of cCSFS was obtained using the threshold method, which resulted in a few non-anatomical connections, e.g., the direct connections between ventricles and the upper parts of the brain.

The non-anatomical connections, which can be classified into obvious and intricate, were cut off using the manual cut-delete type segmentation tools, removing only a minimal portion of cCSFS, just enough to cut the non-anatomical connection (all in 3D Slicer). Obvious non-anatomical connections were identified by visual inspection of the cCSFS segmentation. More subtle intricate connections were detected and removed through an iterative loop in which a CFD solution was computed in COMSOL and the resulting CSF flow and pressure fields were inspected; narrow, non-physiological connections typically produced localized high-pressure gradients, enabling targeted corrections of the cCSFS segmentation in 3D Slicer. This procedure was repeated until the final, anatomically consistent cCSFS segmentation was obtained. The workflow chart is depicted in Figure 1.

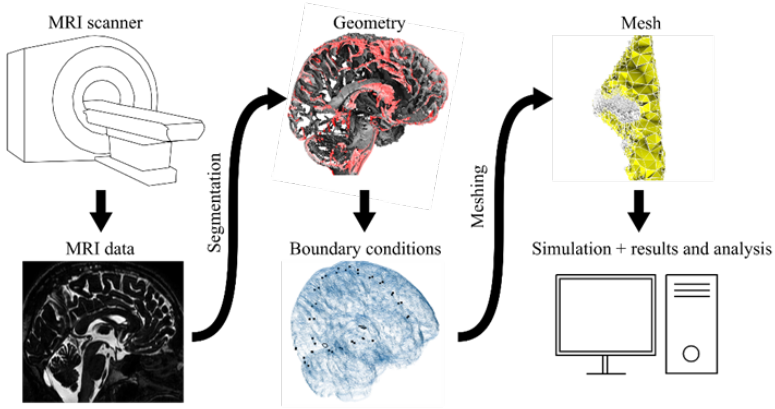

Figure 1. Workflow: 1. MRI data acquisition (MRI scanner, MRI data; grayscale intensity, where brighter values indicate higher signal intensity); 2. Medical image segmentation for patient-specific cranial cerebrospinal fluid (CSF) space (cCSFS) reconstruction (cCSFS shown in grayscale; cut regions shown in pink); 3. Computational fluid dynamics (CFD) model development (cCSFS shown in blue) with boundary conditions for CSF inflow (black loop curves at the choroid plexus) and CSF outflow (black points near the venous sinuses); 4. Computational mesh generation (only the fourth ventricle of the cCSFS is shown here; larger structures are omitted due to high mesh density; the surface mesh is shown in grey, the volumetric mesh in yellow, and mesh edges in white); 5. Simulations resulting in CSF flow fields for further analysis.

2.4. Numerical Model of Steady Net CSF Flow

The objective of the present CFD framework is to predict the steady net redistribution of CSF flow within the MRI reconstructed cCSFS under prescribed CSF production and absorption conditions. In principle, this net component can be obtained by solving the fully transient Navier–Stokes equations with cardiac (and respiratory) forcing and then averaging the pulsatile solution over multiple cycles to obtain a mean "frozen" flow field; for example, averaging over ∼11 cardiac cycles was reported in [7]. For the geometrically detailed cCSFS considered here, such time-resolved simulations would be computationally prohibitive. Moreover, prior analyses indicate that nonlinear convective effects are small in the SAS [23], while the mechanisms by which fast pulsations might contribute to time-averaged CSF drift remain inconclusive [3]. We therefore model the net component directly by solving a stationary, linear effective-flow problem in which the steady pressure field arises as required to satisfy mass conservation for the prescribed CSF sources and sinks. Finally, although the ventricular system is not porous in vivo, we represent the entire cCSFS (ventricles, SAS, and perivascular regions) using an effective Darcy permeability model to predict the net flow distribution and flux partitioning across the full domain; this formulation is not intended to reproduce phase-resolved shear profiles, pulsatility-/respiration-enhanced mixing, or compliance-driven phase lags.

2.4.1. Governing Equations

Based on Darcy's law, the CSF fluid velocity vector, $\mathbf{u}$, in the cSAS and CVS is determined as follows:

$$\mathbf{u} = -\frac{\kappa}{\mu}\nabla p \quad (1)$$

where p is the CSF pressure, ∇p is the CSF pressure gradient, κ is the cSAS and CVS permeability, and μ is the CSF dynamic viscosity.

For the incompressible flow, the continuity equation is as follows:

$$\nabla \cdot \mathbf{u} = 0 \quad (2)$$

where $\nabla\cdot$ is the divergence operator.

2.4.2. CSF Material Parameters

The permeability of the cCSFS was assumed to be uniform and was set to $\kappa = 2.36 \times 10^{-8}$ m^2 [23], while the dynamic viscosity $\mu = 7 \times 10^{-4}$ Pa·s and density $\rho = 993.45$ kg/m^3 of CSF were considered to be those of water.

2.4.3. Boundary Conditions

A reference pressure of 10 mmHg, corresponding to normal intracranial pressure, was imposed at the presumed choroid plexus sites to define the CSF inflow boundary condition [24]. To represent distributed cranial absorption at venous sinus-adjacent sites, sink locations were placed near major dural sinuses. The prescribed net outflow was partitioned such that 80% of sinks were assigned to the superior sagittal sinus (SSS) region and 20% to posterior dural-sinus territories (transverse–sigmoid region near the confluence). This partition is a heuristic intended to avoid unrealistically concentrating all outflow in a single region and to represent that arachnoid granulations are most frequently reported near the SSS but are also commonly observed in posterior sinuses (e.g., transverse/sigmoid and straight sinuses) [25–29].

2.4.4. Mesh

The mesh, representing the cCSFS, was generated with the FEM-based COMSOL Multiphysics® software, and it consisted of more than 19.5 million tetrahedral elements. The mesh element number density was close to 100 tetrahedral elements per 1 mm^3. Due to high mesh density, it was hard to visualize any comparably large anatomical structure; therefore, we only visualize the mesh of a smaller, zoomed-in, anatomical structure of the fourth ventricle, as shown in Figure 1.

2.4.5. Mesh Element Order

The solution accuracy depends on the mesh element order [30]. Tetrahedral finite elements are noted as P. The integration nodes of a first-order P_1 element are located only at the corners, resulting in four nodes per element, while second-order P_2 elements have six additional integration nodes situated in the middle of the edges. The interpolation in P_1 elements is performed using the linear shape functions, while the interpolation on the P_2 element uses the quadratic shape functions.

For general convection–diffusion-driven problems, P_2 mesh elements are expected to be the optimal choice regarding accuracy and computational effort. However, our case differs from the general case, as the surface mesh obtained from the segmentation is extremely dense (surface-to-volume ratio is approximately 1620, which accounts for 20 times more surface area when compared with the sphere of a similar volume). Generally, when the mesh is dense enough, the lower-order elements should provide results comparable

to those of the higher-order elements. Therefore, evaluating whether the element density is high enough to provide accurate results is critical to save significant computation time using first-order P_1 elements.

Two numerical modeling studies were performed to evaluate the differences in solutions and the computational effort required between the P_1 and P_2 order elements. In one study, the mesh was composed only of first-order P_1 elements, and in the second study, only of second-order P_2 elements. In the P_1 case, the mesh resulted in 5.6×10^6 degrees of freedom (DOF), while in the P_2 case, the number of DOF was 3.5×10^7.

2.4.6. Solver Settings

The numerical model of the mean CSF flow was solved with the commercial COMSOL Multiphysics® v6.0 software, which uses the finite element method (FEM) as a basis for the numerical modeling. The stationary solver included the linear iterative Generalized Minimal Residual method (GMRES) solver and the Smoothed Aggregation Algebraic MultiGrid (SAAMG) preconditioner. In addition, SAAMG was combined with Successive Over-Relaxation (SOR) line pre- and post-smoothers and a coarse Parallel Direct Solver (PARDISO). The relative tolerance of the stationary solver was set to 1×10^{-3}.

2.5. Methods for Geometric and CSF Flow Analysis

To analyze CSF flow, we follow a similar procedure developed in [7]. We have calculated projections from the 3D cCSFS model to the 2D xz-plane and then to the 1D z-axis, as shown in Figure 2.

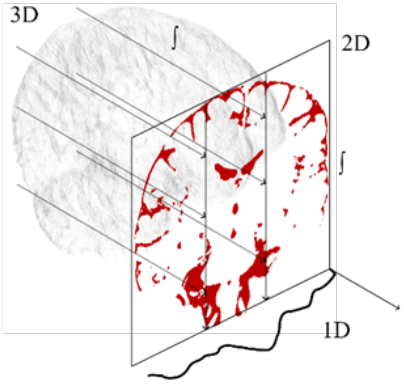

Figure 2. Scheme of the integrating projection operation. The selected parameter is transferred by integrating values along defined projection lines. Two sequential projections are applied to obtain a 1D representation from the original 3D data: first from 3D to 2D along the y-axis (front/back), and then from 2D to 1D along the x-axis (left/right). The cerebral ventricular system (CVS) and subarachnoid space (SAS) regions were analyzed separately.

The z-axis corresponds to the up/down axis, the x-axis to the left/right axis, and the y-axis to the front/back axis. The perimeter was evaluated by slicing the mesh at 1 mm intervals and assessing the length of the resulting curves.

The cCSFS was separated into two parts to evaluate the CSF flow field parameters, the cSAS and CVS. cSAS was composed of the cranial subarachnoid and periarterial spaces (not all periarterial space was reconstructed, as the reconstruction was limited by MRI T_2-weighted resolution). CVS had large regions where the flow was almost zero in the z-axis; therefore, it was filtered by applying $> U_{\text{mean}}$ filter, where U_{mean} is the average CSF flow velocity in CVS, so that it would only include the space where the flow direction is mainly z-axis dominant. In addition, CVS has two regions where the upward flow is dominant in one location and the downward flow is dominant in the other; therefore, the more critical location with the direction of downward flow is used for the flow analysis.

The following operations resulted in a filtered cerebral ventricular system (fCVS) composed of part of third ventricle, aqueduct of Sylvius, and fourth ventricle.

The hydraulic diameter was calculated as $D_{\mathrm{H}} = \frac{4S}{P}$, where S is the cross-sectional area and P is the perimeter of the cross-section. After obtaining D_{H}, the Reynolds number was evaluated as $\mathrm{Re} = \frac{\rho u D_{\mathrm{H}}}{\mu}$.

3. Results

Firstly, we present the geometric parameters of cSAS and fCVS. Secondly, as the numerical simulations of the CSF flow in a cSAS and fCVS are time-demanding tasks, we compare the results obtained with P_1 and P_2 finite elements and show that for this specific problem, the computational time required could be reduced with minimal impact on the solution accuracy by using the P_1 finite elements. Finally, we present the hydrodynamic parameters of the CSF flow in the cSAS and fCVS and analyze the CSF flow results.

3.1. Geometric Parameters

The volume and surface area values presented in Table 1 are obtained from our 3D model of cCSFS.

Table 1. Cranial cerebrospinal fluid space geometric parameters.

Geometric Entity	Volume (mL)	Surface Area (m^2)
Ventricular system	18.3	0.015
Subarachnoid space	180.3	0.307
CSF space (cCSFS)	198.6	0.322

We note that the accuracy of these values is limited by the resolution of tomography imaging (in this case, 3T MRI). The obtained volume values fall into the expected 150–400 mL range [7]. The reconstructed cCSF space has a total surface area of 0.307 m^2. Assuming that half of this area corresponds to the brain-facing boundary yields an effective pial-side area of ∼0.154 m^2, approximately a factor of ∼2 lower than reported high-resolution ex vivo pial-surface measurements. This discrepancy is consistent with the lower spatial resolution of in vivo MRI.

3.2. CSF Flow Simulations

Two stationary numerical simulations of the net CSF flow in the reconstructed cCSFS were performed using P_1 (4 node linear elements) and P_2 (10 node quadratic elements), respectively. The net CSF flow was modeled based on Darcy's law and continuity equations. All simulations were performed on a single Kaunas University of Technology (KTU) cluster node with 2xAMD EPYC 7452 32-core processors and 512 GB of RAM. In both cases, the solution converged in one iteration, and for the P_1 elements, it took almost 5 min, while with the P_2 elements, it took nearly 20 min, consuming about 30 GB of random-access memory (RAM) in the P_1 case and about 150 GB RAM in the P_2 case. Simulations provided the pressure's spatial distribution (field) and its derivative values (velocity, etc.).

3.3. CSF Flow Field Comparison

Several approaches were used to compare the net CSF flow field values obtained by solving the model with P_1 and P_2 elements. Firstly, the three longest streamlines originating in the choroid plexus and following the CSF flow paths in the left, right, and middle brain regions were calculated from the CSF flow solution, which was obtained with P_2 elements. The overall similarity between CSF flow velocity field magnitude values of P_1 and P_2 solutions resulting in these streamlines was evaluated by calculating the correlation

coefficient, mean value proportion, and similarity coefficient based on [31]. The correlation coefficient for the CSF flow velocity field magnitude values [left, right, middle] paths was [0.9932, 0.9964, 0.9967], the mean value proportion was [0.9862, 0.9879, 0.9925], and the similarity coefficient was [0.9635, 0.9728, 0.9701]. All these values indicate substantial similarity between solutions obtained with P_1 and P_2 order elements.

A slight transmantle pressure (the instantaneous pressure difference between the lateral ventricles and the cranial subarachnoid space) value of 1.8 Pa was obtained, which is sufficient to drive the prescribed net CSF flow rate of 500 mL/day, as shown in Figure 3.

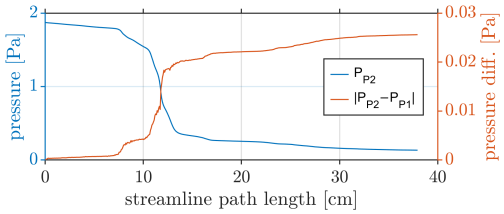

Figure 3. Pressure obtained on the streamline starting at the choroid plexus of the right ventricle and following a path throughout the right-brain hemisphere up to the arachnoid granulations. P_2 solution in blue, difference in pressure between P_2 and P_1 solutions in orange.

The difference between pressures obtained with P_1 and P_2 elements accumulated throughout the CSF flow path, and its increase was proportional to the velocity, as shown in Figure 3. The difference in obtained transmantle pressures was only 1.4% between P_1 and P_2 solutions. Finally, we compared the P_1 and P_2 velocity fields on an element-wise basis. To account for varying element sizes, we evaluated a mass-weighted velocity metric:

$$W_e = m_e \, \|\mathbf{u}_e\| \tag{3}$$

where m_e is the mesh element mass and $\mathbf{u}_e$ is the element-wise CSF velocity. We then computed the relative difference in W_e between the P_1 and P_2 solutions for each element. We found that for 70% of all elements, the difference in W_e was below 5%, for 20%, it ranged from 5% to 10%, and for 10%, it exceeded 10%, as shown in Figure 4.

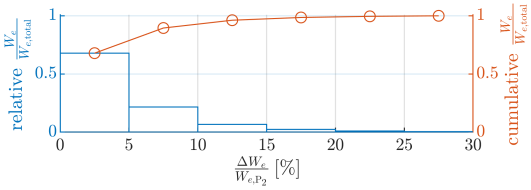

Figure 4. The relative (blue) and cumulative (orange) ratio of mass-weighted velocity metric within the elements, W_e (kg·m/s), with the total system's mass-weighted velocity metric within the elements, between P_1 and P_2 solutions.

To assess whether element-wise discrepancies between the P_1 and P_2 solutions significantly affect global transport, we quantified how much of a mass-weighted transport magnitude is carried by the elements with the largest relative mismatch. The symmetric relative mismatch between the two solutions is then

$$\delta_{e,W} = \frac{\left|W_{e,P_2} - W_{e,P_1}\right|}{\frac{1}{2}\left(\left|W_{e,P_2}\right| + \left|W_{e,P_1}\right|\right) + \varepsilon} \tag{4}$$

and we define a reference transport magnitude

$$W_{e,ref} = \tfrac{1}{2}\left(W_{e,P_1} + W_{e,P_2}\right) \tag{5}$$

After ranking elements by $\delta_{e,W}$ (used only to define the worst-mismatch subset $\Omega_{10\%}$), we quantified their transport-weighted contribution via $S_{10\%}$

$$S_{10\%} = \frac{\sum_{e\in\Omega_{10\%}} |W_{e,\mathrm{ref}}|}{\sum_{e\in\Omega} |W_{e,\mathrm{ref}}|} \quad (6)$$

It was obtained that $S_{10\%} \approx 0.0068$ (i.e., the worst 10% of elements by mismatch account for only ~0.68% of $\sum|W_{\mathrm{ref}}|$), indicating that the largest relative differences are concentrated in low-transport regions and have negligible impact on global net transport metrics.

All these different P_1 and P_2 solution evaluation approaches showed that the differences between the solution obtained with P_1 and P_2 elements are not significant; therefore, for these types of studies, P_1 elements can be used to reduce computational effort and time.

3.4. CSF Flow Analysis

The y-averaged map of the CSF velocity magnitude projected on the xz-plane, U_{xz}, was used to visualize the modeled CSF flow patterns, the distribution of which in fCVS is shown in Figure 5a, while for cSAS, it is shown in Figure 5b. From these patterns it can be deduced that the CSF flow velocity distribution for the fCVS was approximately symmetric around the flow path center (the flow path center is almost parallel to the $x = 0$ axis). In the fCVS, the U_{xz} was highest at the aqueduct of Sylvius and reached about 0.4 cm/s, while in the cSAS, it was highest at specific locations, which forms the CSF up flow from the CVS to the arachnoid granulations. Also, for the cSAS, some local differences of the velocities can be seen between the left and the right brain hemispheres, as the velocities were locally higher in the leftmost part of the brain, as shown in Figure 5b. This can be attributed to local cSAS anatomical differences between brain hemispheres.

The average velocity magnitude in the fCVS was 2×10^{-2} cm/s, while in the cSAS, it was 8×10^{-4} cm/s. Additionally, the average velocity magnitude on the left-brain hemisphere was higher than on the right-brain hemisphere as it was 8.3×10^{-4} cm/s, while on the right-brain hemisphere, it was 7.7×10^{-4} cm/s. As the CSF flow rates were prescribed to be equal between brain hemispheres, the difference in average velocities is due to the difference in cSAS cross-sectional areas between brain hemispheres, as shown in Figure 6. The average cross-sectional area in the main flow direction (z-axis) in cSAS on the left-brain hemisphere was 5.85 cm^2, while on the right-brain hemisphere, it was 6.11 cm^2.

The cross-sectional area of fCVS in z-axis was fluctuating and reached the highest value of almost 0.73 cm^2 at the fourth ventricle and the lowest value of almost 1.6×10^{-2} cm^2 at the aqueduct of Sylvius, as shown in Figure 5c, while cross-sectional area of the cSAS on the z-axis in the cerebrum part of the brain fluctuated around the average value of 15 cm^2, and in the cerebellum part of the brain, it fluctuated around the average value of around 8 cm^2, as shown in Figure 5d. The average cross-sectional area of fCVS was 0.29 cm^2, while of cSAS, it was 12.28 cm^2, resulting in a cross-sectional area ratio cSAS/fCVS of 42.35.

The projected perimeter distributions on the z-axis in principle followed cross-sectional area distribution, as shown in Figure 5c,d, indicating a similar hydraulic diameter throughout the z-axis. This is shown in Figure 5e,f, where the hydraulic diameter for the fCVS was in a range from about 1 to 10 mm with an average value of 5 mm with a comparably low dispersion. The hydraulic diameter in most of the SAS was in a range of about 2 to 4 mm with the average of 3 mm and exhibited low dispersion.

The velocity in the z-axis in the fCVS was from 5×10^{-3} cm/s to almost 0.4 cm/s and the Reynolds number of the CSF flow was in the range from 1 to almost 70, as shown in Figure 5g. The highest velocity and Reynolds number was at the aqueduct of Sylvius, while the lowest velocity and Reynolds number was at the fourth ventricle. The z-component of velocity in the cSAS, where it was relevant, was from around 1×10^{-4} cm/s to 6×10^{-4} cm/s

and the Reynolds number of CSF flow was in the range from 0.05 to 0.3, as shown in Figure 5h. The highest z-component of velocity was at the cerebellum part of the brain. Overall, the dominance of the z-component of the velocity was decreasing towards the arachnoid granulations.

The velocity magnitude in the fCVS was approximate to velocity's z-component and was in the range from 5×10^{-3} cm/s to almost 0.4 cm/s, as shown in Figure 5i. The highest velocity was at the aqueduct of Sylvius, while the lowest velocity was at the fourth ventricle. The velocity magnitude in the cSAS, where it was relevant, was from around 0.5×10^{-3} cm/s to almost 1.5×10^{-3} cm/s, as shown in Figure 5j. The highest velocity magnitude was at the cerebellum part of the brain. The CSF flow velocity in periarterial spaces was nonuniform and when comparing left and right brain sides, it was also non-symmetric, as shown in Figure 7. The average velocity magnitude in periarterial spaces was around 1.5×10^{-3} cm/s, while in the subarachnoid space it was 7.7×10^{-4} cm/s, indicating that periarterial velocities were almost two times higher.

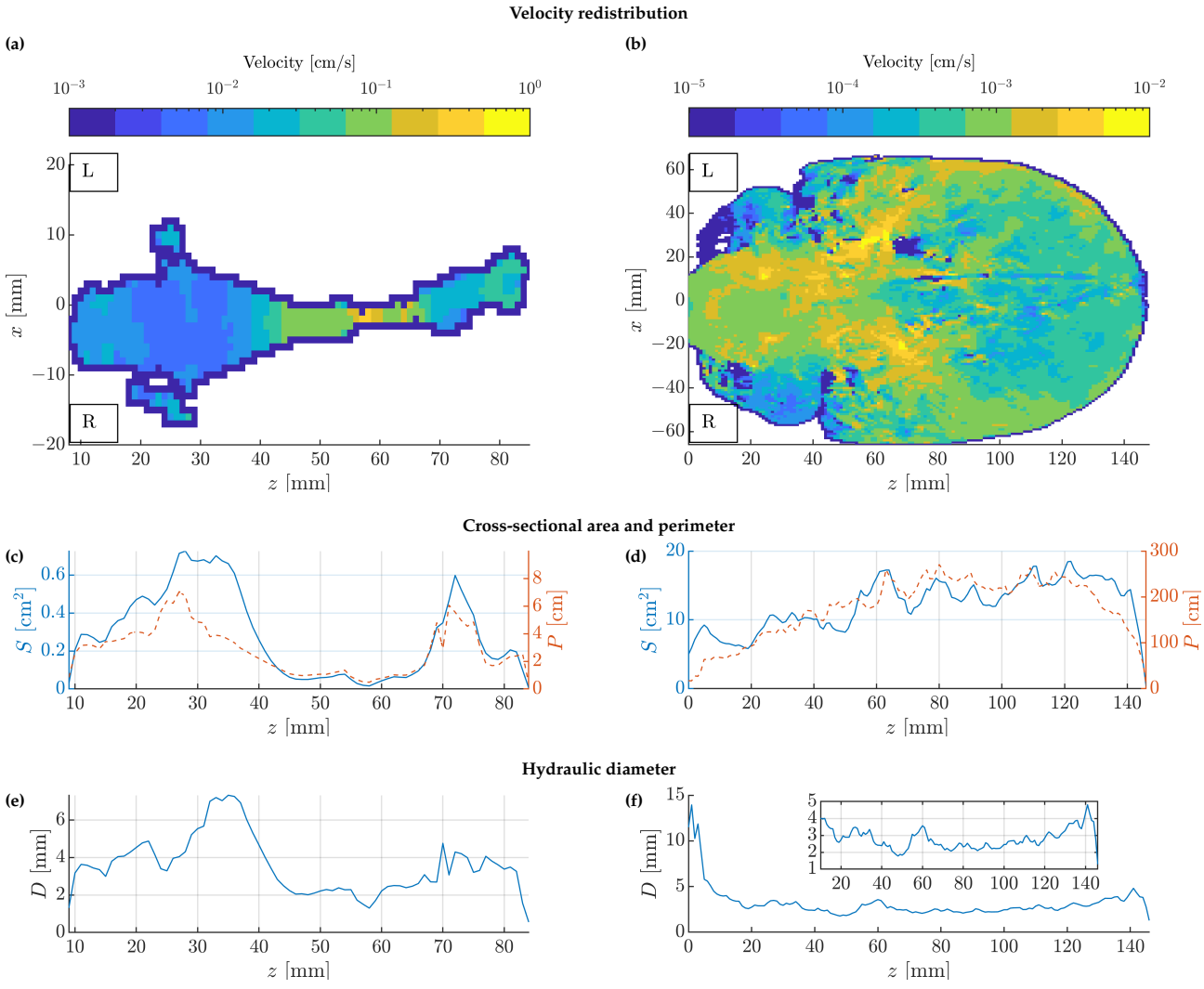

Figure 5. *Cont.*

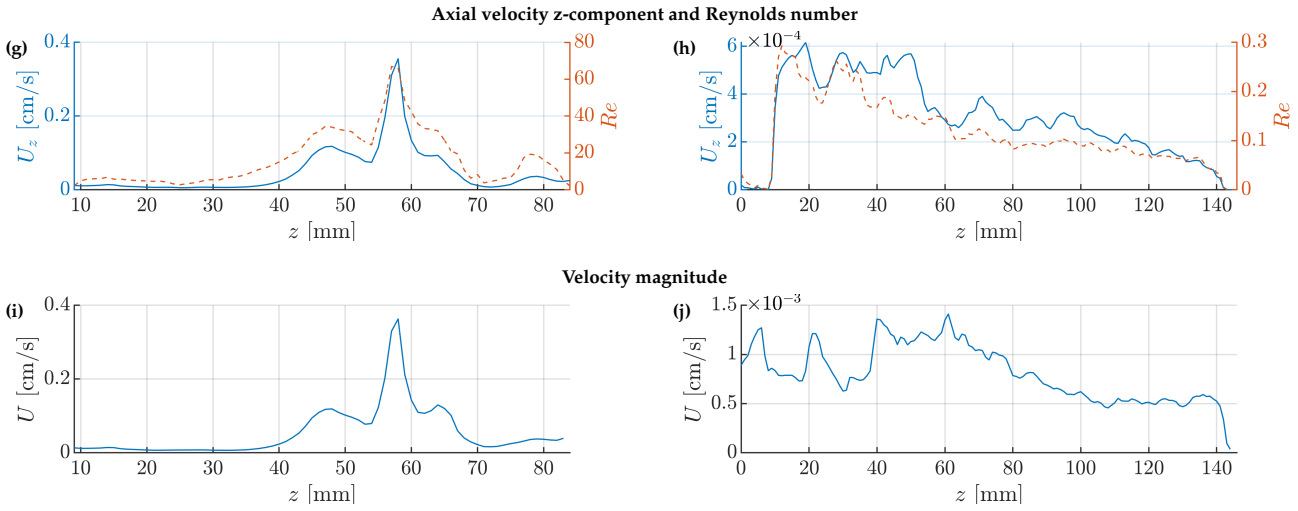

Figure 5. CSF metrics in the filtered cerebral ventricular system (fCVS) and cranial subarachnoid space (cSAS). (**a**,**b**) y-averaged velocity magnitude $\langle|\mathbf{u}|\rangle_y$ on the xz-plane (fCVS, cSAS). (**c**,**d**) Cross-sectional area $S(z)$ (solid) and perimeter $P(z)$ (dashed), integrated over (x, y). (**e**,**f**) Hydraulic diameter $D_{\mathrm{H}}(z) = 4S(z)/P(z)$. (**g**,**h**) Plane-averaged axial velocity $\langle u_z\rangle_{x,y}(z)$ (solid) and Reynolds number $\mathrm{Re}(z)$ (dashed), computed with $D_{\mathrm{H}}(z)$. (**i**,**j**) Plane-averaged velocity magnitude $\langle|\mathbf{u}|\rangle_{x,y}(z)$. Averages are taken over in-domain cross-sections only. Here, $\langle\cdot\rangle_y$ and $\langle\cdot\rangle_{x,y}$ denote averaging over y and over (x, y), respectively.

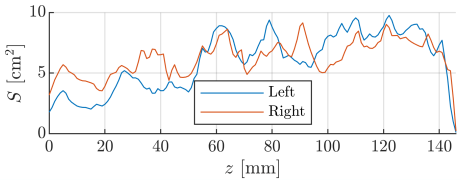

Figure 6. The cross-sectional area of left (solid, blue) and right (solid, orange) hemispheres.

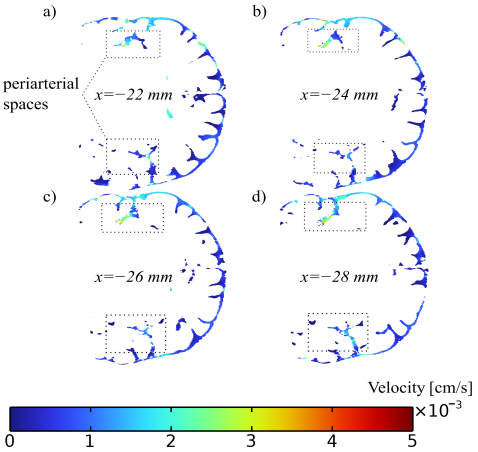

Figure 7. CSF flow magnitude on zy plane at several x locations, where periarterial spaces are present (**a**) at $x = -22$ mm, (**b**) at $x = -24$ mm, (**c**) at $x = -26$ mm, (**d**) at $x = -28$ mm.

4. Discussion

In previous work, it was shown that CSF flow dynamics could have influence on patient outcomes after subarachnoid hemorrhage [32], cerebral ischemia [33], multiple sclerosis [34], or traumatic brain injury [35]. Based on the timely evaluation of the patient-specific CSF flow patterns, clinicians could take appropriate measures to change clinical course and improve patient outcomes. The inclusion of periarterial spaces is important,

especially when considering the clearance of unwanted substances such as leaked blood from the aneurysmal rupture [32]. In addition, periarterial spaces allow for the evaluation of the direct contact between CSF, leaked blood, and artery walls.

The geometry was reconstructed with minimal manual correction to remove non-anatomical connections introduced during segmentation. These interventions were mostly in the areas between ventricles and the parts of the cSAS; however, whether these connections are truly non-anatomical remains to be determined, as some studies on rats indicate that there could be direct connections between ventricles and the cSAS [36].

The obtained surface mesh follows the segmentation of the high resolution T_2-weighted MRI. In most parts, this creates an overly dense mesh, which would lead to the inefficient use of computational power. One way to reduce the density of this mesh is to use surface smoothing procedures. However, any meaningful attempts to smooth out the resulting surface and in this way reduce the geometrical complexity by allowing larger triangles to be used and simultaneously retain sulci and perivascular spaces always leads to the problems of self-intersections and requires the removal of many inside protrusions, making smoothing not applicable. Another option is to reduce the discretization order (P_2 to P_1 as an example) as we did in this paper. The CSF flow results obtained between P_1 and P_2 elements resulted in a difference, which is comparably low, and it is known that given enough mesh density, both solutions should provide similar results [37]. In this paper, we have shown that when using the minimally manually adjusted segmentations directly obtained from the high-resolution MRI, and when using finite element formulations to solve for Darcy flow equations, one can use the P_1 elements and expect a solution that in most parts should be within 10% of relative error from the P_2 solution. In this way, the use of P_1 elements mitigates the computational overhead associated with overly dense meshes in anatomically constrained regions where smoothing cannot reduce geometric complexity. Moreover, uncertainties in CSF flow boundary conditions are at least an order of magnitude larger than the differences between P_1 and P_2 discretizations.

4.1. Indirect Consistency Check Against Reported Physiological Ranges

Because patient-specific, spatially resolved CSF flow measurements were not available for this case, we benchmarked key outputs against reported physiological ranges. This subsection is intended to show that simulated magnitudes are physiologically plausible and to clarify where predictions are most sensitive to modeling assumptions.

4.1.1. CSF Generation/Aqueductal Flow

We prescribe net CSF production rate of 500 mL/day (≈0.35 mL/min). Along the aqueduct, the cross-sectional area ranges from 1.6 to 7.8 mm^2, giving section-averaged mean velocities 0.36–0.075 cm/s, respectively, for a net flow of 0.35 mL/min (by mass conservation). Reported aqueduct-based net production estimates in healthy cohorts are of a similar order: 0.305 ± 0.145 mL/min [38], 0.35 ± 0.38 mL/min [39], 0.205 ± 0.037 mL/min [40], 0.31 ± 0.18 mL/min [41]. Akay [42] reports an aqueduct cross-sectional area of 2.87 ± 1.01 mm^2, a velocity of 0.37 ± 0.18 cm/s, and a flow rate of 0.64 ± 0.40 mL/min in healthy volunteers. Note that net aqueduct estimates of CSF flow can be sensitive to segmentation and physiological confounders such as respiration.

4.1.2. Transmantle Pressure Gradient

Prior modeling generally suggests that time-averaged transmantle pressure differences are small (order 1–10 Pa), while direct human measurements—when attempted—often report values near zero within measurement uncertainty (10 Pa) [43–46]. Our predicted value (1.8 Pa) lies within the low end of these reported ranges.

4.1.3. SAS and Perivascular Drift Velocities

Recent net flow MRI (six healthy subjects) reports no detectable SSS-directed net drift [47]. Under our absorption/outflow assumptions, the model predicts a small mean directed SAS drift velocity of 1×10^{-4} to 6×10^{-4} cm s^{-1} ($\approx$1 to 6 µm s^{-1}). This difference is interpreted as boundary condition and compartment assumption-sensitive, rather than a direct contradiction, because net flow MRI targets ultraslow signed drift, while periarterial/perivascular pathways can exhibit preferential transport with larger local velocities. In our model, local PVS velocities are in the range of 10–100 µm/s (Figure 5b). Tracer MRI additionally suggests a periarterial SAS compartment (PVSAS) separated by a semipermeable boundary with preferential periarterial tracer propagation [48], although observed enhancement patterns may also be influenced by shear-augmented dispersion under oscillatory flow [49].

4.1.4. Effective SAS Cross-Sectional Area

An imaging-based estimate of six healthy subjects reports an effective SAS cross-section 14.55 to 25.79 cm^2 [47], whereas our estimate is 12.28 cm^2. This discrepancy likely reflects differences in segmentation definitions (which SAS regions are included) and resolution/continuity assumptions; we therefore treat this comparison as an order-of-magnitude plausibility check.

4.1.5. Cranial SAS Pial-Side Surface Area Comparison with Ex Vivo Measurements

Our reconstructed cranial SAS has a total surface area of 0.307 m^2, which includes both "brain-facing" (pial-adjacent) and "dura-facing" boundaries. As a rough pial-side comparator, half of this value ($\sim$0.154 m^2) can be interpreted as an effective brain-facing area. High-resolution, ex vivo reconstructions report combined cerebrum and cerebellum pial surface areas of $\sim$0.363 m^2 [50], whereas our estimate is derived from in vivo clinical MRI, where spatial resolution and partial-volume effects under-resolve thin sulcal/folial CSF boundaries. This comparison therefore indicates the expected discrepancy in pial-adjacent surface area when estimated from in vivo MRI segmentation (here, on the order of a factor of $\sim$2). Such discrepancy is relevant for models that scale CSF–tissue exchange/transport processes by interface area (e.g., solute diffusion/uptake, intrathecal drug penetration, or coupling between SAS and perivascular/interstitial compartments).

4.1.6. Comparison with Other Modeling Works

Although several CFD studies have investigated CSF dynamics in the SAS [8,10,11], only in [7] were geometric and hydrodynamic summary metrics reported that enable partial, order-of-magnitude comparison with our results. Here, we compare time-averaged transport scales: in [7] a steady-streaming component (oscillatory pulsations superimposed with net sources/sinks) was computed, whereas our model solves only a steady-state problem driven by prescribed CSF generation and absorption boundary conditions. This comparison is meaningful at the level of orders of magnitude for time-averaged transport, but remains limited by differing pulsatility assumptions, boundary conditions, and geometric preprocessing, and thus does not constitute strict model-to-model validation.

Geometrically, our cranial subarachnoid space (cSAS) spans cross-sectional areas of 5 to 19 cm^2, perimeters of 10 to 250 cm, and hydraulic diameters of 1.9 to 14 mm (mean: 3 mm). In comparison, ref. [7] reports 4 to 31 cm^2, 10 to 190 cm, and 5.2 to 11.5 mm (mean: 6.2 mm) over the cSAS, respectively. The approximately two-fold difference in mean hydraulic diameter (our 3 mm vs. their 6.2 mm) is mainly attributable to their geometric smoothing/coarsening steps designed to enforce SAS continuity, whereas we retained the

MRI-derived geometry with minimal interventions; regions that appear discontinuous in our model are typically below MRI resolution and would, if included, further reduce D_h.

In terms of transport magnitude, the cranial steady-streaming is 50× smaller than spinal [7], implying a cranial drift on the order of 0.5–0.7 µm/s (approximate estimate from their reported spinal steady-streaming), whereas we obtain steady flow velocity of 1–6 µm/s in cSAS; both are in the µm/s regime and therefore far below peak oscillatory CSF speeds. Finally, our steady component remains strongly viscosity dominated (cSAS Re $\leq$ 0.2, Figure 5h), consistent with [7] showing near-zero Re in cranial regions.

4.2. Implications of Neglecting Pulsatility, Respiration, and Compliance When Modeling CSF Flow

Our model is formulated to predict the steady net component of CSF redistribution driven by prescribed CSF production and absorption rates and sites, with pressure arising as the corresponding steady field required to satisfy mass conservation. It is therefore not intended to reproduce phase-resolved oscillatory waveforms, pulsatility-enhanced mixing, respiratory modulation, or compliance-driven phase lags. Nonetheless, periarterial/PVS flow is strongly cardiac-coupled. In vivo two-photon particle tracking in mice demonstrated a pulsatile periarterial component synchronized to heartbeat and reported a time-averaged (net) bulk-flow speed in pial-artery PVS of ~18.7 µm/s directed along the artery [51]. Consistent with this benchmark, our predicted mean periarterial CSF velocity was 1.5×10^{-3} cm/s (15 µm/s), i.e., of the same order as the mouse time-averaged value. In addition, particle-tracking experiments in mice have reported a pulsatile periarterial CSF motion with a non-zero mean ("bulk flow") component aligned with the direction of blood flow. This directed component persists under a dual-syringe infusion protocol with simultaneous injection and withdrawal (no net volume increase and minimal ICP change), arguing against a simple injection-driven artifact [52]. In humans, motion-sensitive MRI supports robust cardiac cycle coupling between vascular pulsatility and paravascular CSF dynamics, based on retrospectively cardiac-aligned fMRI and dynDWI waveforms [53]. Velocity-selective spin labeling (VSSL) has further been used to map CSF motion in the ventricles and along major-artery regions of the SAS [54]. However, these measurements primarily characterize pulsatile and/or velocity magnitude-weighted motion components and therefore should not be interpreted as direct estimates of the cycle-averaged signed net drift within anatomically defined PVS.

Because we focus on the steady net CSF flow, the key question is whether neglecting time dependence biases the predicted net drift. Direct in vivo measurements of the net flow velocity specifically within human PVS remain limited. Importantly, time-dependent CFD in realistic pial PVS geometries indicates that arterial wall expansion can generate large oscillatory velocities (peak-to-peak amplitudes on the order of 60–265 µm/s), yet pulsations alone may yield negligible mean drift in physiologically short geometries (net < 0.5 µm/s, and still <0.2 µm/s when adding downstream resistance/compliance) [2]. In that setting, pulsatility predominantly contributes to oscillatory motion and mixing rather than to time-averaged transport, supporting the use of a steady net flow model when the mean is governed by steady drivers [2]. Conversely, the same framework shows that a static pressure gradient can dominate the mean: for a static gradient of 1.46 mmHg/m, predicted net velocities are ~20–30 µm/s, while the oscillatory peak-to-peak amplitude remains essentially unchanged [2]. These results motivate the interpretation that, even in strongly pulsatile PVS, the cycle-averaged drift may be set primarily by steady biases (sources/sinks and/or an effective steady pressure difference), with pulsatility superimposed on top [2].

Evidence from human intrathecal tracer MRI indicates brain-wide redistribution and clearance over time, including enhancement patterns consistent with vessel-adjacent pathways [55], while sleep deprivation impairs molecular clearance [56], suggesting that

CSF-mediated transport is state-dependent. However, rapid tracer redistribution does not uniquely imply a large net drift because oscillatory motion can substantially enhance solute transport via shear-augmented dispersion even in the absence of net bulk flow [49]. Consistent with the relevance of low-frequency dynamics, sleep cycle-dependent vasomotion has been shown to modulate vascular/PVS dynamics in mice and is predicted to increase perivascular flow and solute transport to levels comparable to cardiac-driven oscillations [57].

Rectification becomes relevant only if nominally zero-mean oscillations are converted into non-zero mean flow by symmetry-breaking mechanisms (e.g., direction-dependent hydraulic resistance/valves, geometric asymmetry, or nonlinear compliance/phase lag). Valve mechanism models, for example, propose pressure-dependent permeability at astrocyte endfeet that suppresses reflux and can rectify pulsatile motion into a directed mean flow [58]. At present, however, the mechanism producing the observed net movement remains unsettled, and consensus on how fast pulsations relate to slow time-averaged bulk motion remains elusive [2,59]. Accordingly, our steady model should be interpreted as a tool for studying how prescribed steady drivers shape net CSF flow redistribution, while acknowledging that any additional mean contribution arising from oscillation-rectifying mechanisms would require explicit time-dependent modeling with appropriate asymmetry and compliance.

4.3. Clinical Integration Considerations

In its current proof-of-concept form, the framework is best positioned as an offline research-stage decision-support concept for elective assessment (same-day to next-day), rather than an acute bedside tool. A plausible clinical workflow would include the following:

Imaging inputs: A structural MR dataset with sufficient CSF–tissue contrast and resolution for the segmentation of ventricles and cranial SAS, ideally sub-millimeter isotropic or near-isotropic resolution. Optional additions for personalization include (a) TOF-MRA/CTA to localize major arterial trees and (b) PC-MRI planes (aqueduct and/or foramen magnum) to constrain net flow and pulsatility where available.

Processing pipeline: DICOM import → automated/semi-automated segmentation (ventricles/SAS and PVS) → segmentation quality control (QC) and minor edits → mesh generation → steady solver run → results QC (e.g., checking mass balance, unrealistic velocities, sensitivity to boundary settings; if QC fails, segmentation/mesh are revised and the solver is re-run) → final export of velocity/pressure fields, summary metrics (tables/plots), and image overlays.

Computational resources: The current steady-state formulation is CPU-tractable on a modern workstation/server; practical bottlenecks are segmentation, QC, and mesh generation rather than the linear solve. A GPU is beneficial mainly for AI-based segmentation. The CFD step typically gains little from a GPU in standard CFD because it relies on sparse linear algebra and meshing workflows that are commonly CPU-based in mainstream solvers.

Turnaround time: In the current research implementation, end-to-end time is dominated by segmentation/QC and meshing, so turnaround is realistically hours to days, not minutes. With improved automation (robust segmentation and repeatable meshing settings/templates), the workflow could support elective planning where a turnaround of hours is acceptable; at this stage, it is not intended for emergency decision-making.

User expertise: At present, operation requires a trained user with experience in medical image segmentation and computational modeling to verify that the segmented CSF compartments are anatomically consistent and free of artifacts (e.g., missing regions, spurious connections, or non-physical gaps), verify meshing and boundary condition

settings, and interpret QC flags. Clinical deployment would require a streamlined "single-operator" interface with locked presets, automated QC checks, and standardized reporting.

5. Limitations

This study presents a proof-of-concept, geometrically detailed framework for patient-specific CSF flow modeling. The next step is evaluation in larger cohorts, including pathological cases such as SAH, hydrocephalus and brain tumors, which will require disease-specific model adaptations (e.g., revised boundary/initial conditions and inclusion of additional mechanisms). Future work should also test whether inter-subject variability in CSF-space geometry (SAS/PVS caliber, continuity, connectivity) produces systematic transport differences that are associated with disease susceptibility or progression (e.g., hydrocephalus, impaired clearance after SAH).

A major limitation of the present work is the lack of patient-specific, spatially resolved CSF flow measurements that would enable direct quantitative validation across the ventricles, SAS, and perivascular regions. Practically, whole-brain in vivo validation is constrained by current MRI capabilities: phase-contrast MRI (PC-MRI) is most commonly acquired on selected 2D planes rather than as a whole-brain 3D field, and scan time and spatial resolution can limit accuracy, particularly for slow flows and small compartments [60]. Accordingly, our benchmarking is limited to indirect consistency checks against published physiological ranges rather than case-specific validation. In addition, model prediction of net SAS drift velocity is sensitive to the assumed CSF absorption/outflow boundary conditions (e.g., "classical" arachnoid granulation–dominated clearance) and a lack of PVSAS compartmentalization (even though we included PVS in our model it shares the same compartment as SAS). Finally, the geometric representation of PVS (caliber and continuity) can change how easily CSF can pass through them compared with the surrounding SAS. If the modeled PVS are relatively "open" and well connected, the simulation may route more CSF through the PVS, which can alter the predicted flow directions and velocities. Moreover, clinical T_2-weighted MRI under-resolves small PVS (partial-volume effects), which can bias reconstructed PVS caliber/continuity and thereby alter predicted routing.

In addition, subject-specific data to constrain regional net flow partitioning are limited. In the absence of such constraints, we assumed an 80%/20% upper/lower partitioning of the net flow and hemispheric symmetry; these should be interpreted as simplifying boundary condition assumptions rather than experimentally established subject-specific values.

Another limitation is that we model the entire cranial CSF domain using Darcy flow with a uniform isotropic permeability (adopted from a trabecular SAS porous-medium estimate) [23]. Applying this single value to anatomically heterogeneous regions (ventricles, cisterns, and larger periarterial conduits) is an effective approximation that may bias hydraulic resistance and flux partitioning. In particular, Darcy flow does not capture shear, velocity gradients, or pulsatility-driven mixing that are expected in open-fluid regions; these effects would require Stokes/Navier–Stokes modeling and compliant/pulsatile boundary conditions. This simplification is particularly relevant because periarterial spaces have been reported to be open (non-porous) conduits in mice [61], and computational studies indicate that geometric differences between periarterial and perivenous pathways can substantially affect net transport [6].

In addition, CSF sink placement was limited to the SSS and transverse–sigmoid territories; we did not include a dedicated straight-sinus sink region despite reports of frequent arachnoid granulations in the straight sinus, which may affect regional outflow partitioning and should be addressed in future sensitivity analyses.

A central limitation for next-generation patient-specific CSF models is the incomplete mechanistic understanding of what sets net CSF redistribution in humans—specifically, how

steady production/absorption and outflow resistances interact with pulsatility/respiration, compliance, and periarterial compartmentalization to produce the observed net tracer transport pathways. Until these drivers are better constrained by spatially resolved in vivo measurements, model boundary conditions and net flow mechanisms will remain partly assumption-driven.

6. Conclusions

This work presents a patient-specific FEM framework for studying steady net CSF redistribution in a cranial CSF domain reconstructed from T_2-weighted MRI (ventricular system, cranial SAS, and periarterial regions). We further show that the computational cost of this large-scale steady problem can be reduced with only minor impact on the solution by using first-order elements instead of second-order elements.

Using a steady Darcy formulation with prescribed net CSF production/absorption of 500 mL/day (≈0.35 mL/min), the model predicts a small transmantle pressure difference ($\Delta p \approx 1.8$ Pa) and micro-scale steady net CSF flow velocities (periarterial: 1.5×10^{-3} cm/s; cSAS: 8×10^{-4} cm/s). Given the reconstructed aqueduct cross-sectional area (1.6–7.8 mm^2), the implied aqueductal mean velocity scale (≈0.36–0.075 cm/s), respectively, is consistent with reported PC-MRI ranges, and the transmantle pressure difference lies within the (<10 Pa) range reported by prior modeling studies. Because these results describe steady net CSF transport under a prescribed production rate and chosen absorption/outflow boundaries (a classical steady source–sink setting), predicted net flow directionality should be interpreted as conditional on these assumptions and used as a mechanistic baseline rather than a clinically validated ground truth. Next steps are evaluation in larger cohorts (including SAH, hydrocephalus, brain tumors), with disease-adapted boundary/initial conditions and mechanisms, and assessment of whether inter-subject differences in SAS/PVS geometry (caliber, continuity, connectivity) produce systematic transport patterns relevant to disease susceptibility or progression.

Author Contributions: Conceptualization, E.M., A.D., A.P. and V.P.; methodology, E.M., A.D., A.P., T.I., J.S. and V.R.; software, E.M. and T.I.; validation, E.M., A.D., A.P., A.B., V.R., R.A., S.L., M.Š., I.L. and V.P.; formal analysis, E.M., A.D., A.P., G.S., R.N., R.A. and V.P.; investigation, E.M.; resources, A.P., V.R., A.B., R.A. and S.L.; data curation, A.P. and S.L.; writing—original draft preparation, E.M.; writing—review and editing, E.M., A.D., V.P. and A.P.; visualization, E.M.; supervision, A.D. and V.P.; project administration, V.P.; funding acquisition, E.M. and V.P. All authors have read and agreed to the published version of the manuscript.

Funding: This research was supported by the Research Council of Lithuania (RCL) through the Projects of Postdoctoral Fellowships funded by the state budget of the Republic of Lithuania (Project No. S-PD-24-117).

Institutional Review Board Statement: The study was conducted in accordance with the Declaration of Helsinki and approved by the Vilnius Regional Biomedical Research Ethics Committees (Protocol No. BE-2-113 on 9 September 2021 and 2021/9-1370-847 on 21 September 2021) during September 2021–August 2024. The study was registered at the Protocol registration results system, ClinicalTrials.gov (ID NCT06006975).

Informed Consent Statement: Informed consent was obtained from all subjects for the use of their anonymized clinical data in the analysis and publication of this paper.

Data Availability Statement: The datasets used and analyzed during the current study are available from the corresponding author upon reasonable request.

Conflicts of Interest: V. Petkus, A. Džiugys, A. Preikšaitis, E. Misiulis, G. Skarbalius, R. Navakas, T. Iešmantas, M. Šerpytis, S. Lukoševičius, V. Ratkūnas, A. Barkauskienė, I. Lapinskienė, and R. Alzbutas have patent pending for invention related to a method for the early warning of cerebral vasospasm after subrachnoid hemorrhage based on numerical modeling of cerebrospinal fluid flow.

References

1. Ladrón-de-Guevara, A.; Shang, J.K.; Nedergaard, M.; Kelley, D.H. Perivascular pumping in the mouse brain: Improved boundary conditions reconcile theory, simulation, and experiment. *J. Theor. Biol.* **2022**, *542*, 111103. [CrossRef]
2. Daversin-Catty, C.; Vinje, V.; Mardal, K.A.; Rognes, M.E. The mechanisms behind perivascular fluid flow. *PLoS ONE* **2020**, *15*, e0244442. [CrossRef]
3. Kedarasetti, R.T.; Drew, P.J.; Costanzo, F. Arterial pulsations drive oscillatory flow of CSF but not directional pumping. *Sci. Rep.* **2020**, *10*, 10102. [CrossRef] [PubMed]
4. Asgari, M.; de Zélicourt, D.; Kurtcuoglu, V. Glymphatic solute transport does not require bulk flow. *Sci. Rep.* **2016**, *6*, 38635. [CrossRef]
5. Yokoyama, N.; Takeishi, N.; Wada, S. Cerebrospinal fluid flow driven by arterial pulsations in axisymmetric perivascular spaces: Analogy with Taylor's swimming sheet. *J. Theor. Biol.* **2021**, *523*, 110709. [CrossRef] [PubMed]
6. Vinje, V.; Bakker, E.N.T.P.; Rognes, M.E. Brain solute transport is more rapid in periarterial than perivenous spaces. *Sci. Rep.* **2021**, *11*, 16085. [CrossRef] [PubMed]
7. Khani, M.; Sass, L.R.; Sharp, M.K.; McCabe, A.R.; Zitella Verbick, L.M.; Lad, S.P.; Martin, B.A. In vitro and numerical simulation of blood removal from cerebrospinal fluid: Comparison of lumbar drain to Neurapheresis therapy. *Fluids Barriers CNS* **2020**, *17*, 16. [CrossRef]
8. Tangen, K.; Narasimhan, N.S.; Sierzega, K.; Preden, T.; Alaraj, A.; Linninger, A.A. Clearance of subarachnoid hemorrhage from the cerebrospinal fluid in computational and in vitro models. *Ann. Biomed. Eng.* **2016**, *44*, 3478–3494. [CrossRef]
9. Khani, M.; Sass, L.R.; McCabe, A.R.; Zitella Verbick, L.M.; Lad, S.P.; Sharp, M.K.; Martin, B.A. Impact of Neurapheresis System on intrathecal cerebrospinal fluid dynamics: A computational fluid dynamics study. *J. Biomech. Eng.* **2020**, *142*, 021006. [CrossRef]
10. Vandenbulcke, S.; De Pauw, T.; Dewaele, F.; Degroote, J.; Segers, P. Computational fluid dynamics model to predict the dynamical behavior of the cerebrospinal fluid through implementation of physiological boundary conditions. *Front. Bioeng. Biotechnol.* **2022**, *10*, 1040517. [CrossRef]
11. Khani, M.; Burla, G.K.R.; Sass, L.R.; Arters, O.N.; Xing, T.; Wu, H.; Martin, B.A. Human in silico trials for parametric computational fluid dynamics investigation of cerebrospinal fluid drug delivery: Impact of injection location, injection protocol, and physiology. *Fluids Barriers CNS* **2022**, *19*, 8. [CrossRef] [PubMed]
12. Sincomb, S.J.; Coenen, W.; Criado-Hidalgo, E.; Wei, K.; King, K.; Borzage, M.; Haughton, V.; Sánchez, A.L.; Lasheras, J.C. Transmantle pressure computed from MR imaging measurements of aqueduct flow and dimensions. *Am. J. Neuroradiol.* **2021**, *42*, 1815–1821. [CrossRef]
13. Vandenbulcke, S.; Condron, P.; Safaei, S.; Holdsworth, S.; Degroote, J.; Segers, P. A computational fluid dynamics study to assess the impact of coughing on cerebrospinal fluid dynamics in Chiari type 1 malformation. *Sci. Rep.* **2024**, *14*, 12717. [CrossRef]
14. Fillingham, P.; Levendovszky, S.R.; Andre, J.; Parsey, C.; Bindschadler, M.; Friedman, S.; Kurt, M.; Aliseda, A.; Levitt, M.R. Patient-specific computational fluid dynamic simulation of cerebrospinal fluid flow in the intracranial space. *Brain Res.* **2022**, *1790*, 147962. [CrossRef] [PubMed]
15. Fillingham, P.; Kurt, M.; Rane Levendovszky, S.; Levitt, M.R. Computational fluid dynamics of cerebrospinal fluid. In *Computational Neurosurgery, Advances in Experimental Medicine and Biology*; Springer: Cham, Switzerland, 2024; Volume 1462, pp. 417–434. [CrossRef]
16. Saboori, P.; Sadegh, A. Histology and morphology of the brain subarachnoid trabeculae. *Anat. Res. Int.* **2015**, *2015*, 279814. [CrossRef]
17. Wardlaw, J.M.; Benveniste, H.; Nedergaard, M.; Zlokovic, B.V.; Mestre, H.; Lee, H.; Doubal, F.N.; Brown, R.; Ramirez, J.; MacIntosh, B.J.; et al. Perivascular spaces in the brain: Anatomy, physiology and pathology. *Nat. Rev. Neurol.* **2020**, *16*, 137–153. [CrossRef] [PubMed]
18. Macdonald, R.L.; Schweizer, T.A. Spontaneous subarachnoid haemorrhage. *Lancet* **2017**, *389*, 655–666. [CrossRef]
19. Walid, M.S.; Sahiner, G.; Robinson, D.R.; Robinson, J.S. The relationship between pulmonary dysfunction and age in vasospasm patients receiving triple H therapy. *J. Vasc. Interv. Neurol.* **2011**, *4*, 29–33.
20. Fedorov, A.; Beichel, R.; Kalpathy-Cramer, J.; Finet, J.; Fillion-Robin, J.-C.; Pujol, S.; Bauer, C.; Jennings, D.; Fennessy, F.; Sonka, M.; et al. 3D Slicer as an image computing platform for the Quantitative Imaging Network. *Magn. Reson. Imaging* **2012**, *30*, 1323–1341. [CrossRef]
21. Kikinis, R.; Pieper, S.D.; Vosburgh, K.G. 3D Slicer: A platform for subject-specific image analysis, visualization, and clinical support. In *Intraoperative Imaging and Image-Guided Therapy*; Springer: New York, NY, USA, 2014; pp. 277–289. [CrossRef]

22. COMSOL AB. *COMSOL Multiphysics®*, v. 6.0; COMSOL AB: Stockholm, Sweden, 2022. Available online: https://www.comsol.com (accessed on 22 October 2025).
23. Gupta, S.; Soellinger, M.; Boesiger, P.; Poulikakos, D.; Kurtcuoglu, V. Three-dimensional computational modeling of subject-specific cerebrospinal fluid flow in the subarachnoid space. *J. Biomech. Eng.* **2009**, *131*, 021010. [CrossRef]
24. Wan, J.; Zhou, S.; Mea, H.J.; Guo, Y.; Ku, H.; Urbina, B.M. Emerging roles of microfluidics in brain research: From cerebral fluids manipulation to brain-on-a-chip and neuroelectronic devices engineering. *Chem. Rev.* **2022**, *122*, 7142–7181. [CrossRef]
25. Grzybowski, D.M.; Herderick, E.E.; Kapoor, K.G.; Holman, D.W.; Katz, S.E. Human Arachnoid Granulations Part I: A Technique for Quantifying Area and Distribution on the Superior Surface of the Cerebral Cortex. *Fluids Barriers CNS* **2007**, *4*, 6. [CrossRef]
26. Kaplanoğlu, V.; Kaplanoğlu, H.; Turan, A.; Dilli, A. Evaluation of Arachnoid Granulations in Cranial Dural Sinuses with Contrast-Enhanced 3-Dimensional T1-Weighted Magnetic Resonance Imaging. *Eurasian J. Med.* **2023**, *55*, 95–99. [CrossRef] [PubMed]
27. Radoš, M.; Živko, M.; Periša, A.; Orešković, D.; Klarica, M. No Arachnoid Granulations—No Problems: Number, Size, and Distribution of Arachnoid Granulations From Birth to 80 Years of Age. *Front. Aging Neurosci.* **2021**, *13*, 698865. [CrossRef]
28. Liang, L.; Korogi, Y.; Sugahara, T.; Ikushima, I.; Shigematsu, Y.; Takahashi, M.; Provenzale, J.M. Normal Structures in the Intracranial Dural Sinuses: Delineation with 3D Contrast-Enhanced Magnetization Prepared Rapid Acquisition Gradient-Echo Imaging Sequence. *AJNR Am. J. Neuroradiol.* **2002**, *23*, 1739–1746.
29. Haroun, A.A.; Mahafza, W.S.; AlNajar, M.S. Arachnoid Granulations in the Cerebral Dural Sinuses as Demonstrated by Contrast-Enhanced 3D Magnetic Resonance Venography. *Surg. Radiol. Anat.* **2007**, *29*, 323–328. [CrossRef] [PubMed]
30. Eller, D. Fast, unstructured-mesh finite-element method for nonlinear subsonic flow. *J. Aircr.* **2012**, *49*, 1471–1479. [CrossRef]
31. Džiugys, A.; Navakas, R.; Striūgas, N. A normalized parameter for similarity/dissimilarity characterization of sequences. *Informatica* **2015**, *26*, 241–258. [CrossRef]
32. Zhou, J.; Guo, P.; Guo, Z.; Sun, X.; Chen, Y.; Feng, H. Fluid metabolic pathways after subarachnoid hemorrhage. *J. Neurochem.* **2022**, *160*, 13–33. [CrossRef]
33. Mestre, H.; Du, T.; Sweeney, A.M.; Liu, G.; Samson, A.J.; Peng, W.; Mortensen, K.N.; Stæger, F.F.; Bork, P.A.; Bashford, L.; et al. Cerebrospinal fluid influx drives acute ischemic tissue swelling. *Science* **2020**, *367*, 1198–1199. [CrossRef]
34. Rammohan, K. Cerebrospinal fluid in multiple sclerosis. *Ann. Indian Acad. Neurol.* **2009**, *12*, 246. [CrossRef]
35. Zetterberg, H.; Smith, D.H.; Blennow, K. Biomarkers of mild traumatic brain injury in cerebrospinal fluid and blood. *Nat. Rev. Neurol.* **2013**, *9*, 201–210. [CrossRef]
36. Magdoom, K.N.; Brown, A.; Rey, J.; Mareci, T.H.; King, M.A.; Sarntinoranont, M. MRI of whole rat brain perivascular network reveals role for ventricles in brain waste clearance. *Sci. Rep.* **2019**, *9*, 11480. [CrossRef] [PubMed]
37. McCarthy, M.A.; McCarthy, C.T.; Lawlor, V.P.; Stanley, W.F. Three-dimensional finite element analysis of single-bolt, single-lap composite bolted joints: Part I—model development and validation. *Compos. Struct.* **2005**, *71*, 140–158. [CrossRef]
38. Huang, T.-Y.; Chung, H.-W.; Chen, M.-Y.; Giiang, L.-H.; Chin, S.-C.; Lee, C.-S.; Chen, C.-Y.; Liu, Y.-J. Supratentorial Cerebrospinal Fluid Production Rate in Healthy Adults: Quantification with Two-Dimensional Cine Phase-Contrast MR Imaging with High Temporal and Spatial Resolution. *Radiology* **2004**, *233*, 603–608. [CrossRef]
39. Takahashi, H.; Tanaka, H.; Fujita, N.; Murase, K.; Tomiyama, N. Variation in Supratentorial Cerebrospinal Fluid Production Rate in One Day: Measurement by Nontriggered Phase-Contrast Magnetic Resonance Imaging. *Jpn. J. Radiol.* **2011**, *29*, 110–115. [CrossRef]
40. Lindstrøm, E.K.; Ringstad, G.; Mardal, K.-A.; Eide, P.K. Cerebrospinal Fluid Volumetric Net Flow Rate and Direction in Idiopathic Normal Pressure Hydrocephalus. *NeuroImage Clin.* **2018**, *20*, 731–741. [CrossRef]
41. Spijkerman, J.M.; Geurts, L.J.; Siero, J.C.W.; Hendrikse, J.; Luijten, P.R.; Zwanenburg, J.J.M. Phase Contrast MRI Measurements of Net Cerebrospinal Fluid Flow through the Cerebral Aqueduct Are Confounded by Respiration. *J. Magn. Reson. Imaging* **2019**, *49*, 433–444. [CrossRef] [PubMed]
42. Akay, R.; Kamisli, O.; Kahraman, A.; Oner, S.; Tecellioglu, M. Evaluation of Aqueductal CSF Flow Dynamics with Phase Contrast Cine MR Imaging in Idiopathic Intracranial Hypertension Patients: Preliminary Results. *Eur. Rev. Med. Pharmacol. Sci.* **2015**, *19*, 3475–3479.
43. Jacobson, E.E.; Fletcher, D.F.; Morgan, M.K.; Johnston, I.H. Fluid Dynamics of the Cerebral Aqueduct. *Pediatr. Neurosurg.* **1996**, *24*, 229–236. [CrossRef]
44. Fin, L.; Grebe, R. Three Dimensional Modeling of the Cerebrospinal Fluid Dynamics and Brain Interactions in the Aqueduct of Sylvius. *Comput. Methods Biomech. Biomed. Eng.* **2003**, *6*, 163–170. [CrossRef]
45. Linninger, A.A.; Xenos, M.; Zhu, D.C.; Somayaji, M.B.R.; Kondapalli, S.; Penn, R.D. Cerebrospinal Fluid Flow in the Normal and Hydrocephalic Human Brain. *IEEE Trans. Biomed. Eng.* **2007**, *54*, 291–302. [CrossRef]
46. Masoumi, N.; Framanzad, F.; Zamanian, B.; Seddighi, A.S.; Moosavi, M.H.; Najarian, S.; Bastani, D. 2D Computational Fluid Dynamic Modeling of Human Ventricle System Based on Fluid–Solid Interaction and Pulsatile Flow. *Basic Clin. Neurosci.* **2013**, *4*, 64–75.

47. van der Voort, E.C.; van der Plas, M.C.E.; Gosselink, M.W.J.M.; Zwanenburg, J.J.M. Challenging the Classical View of CSF Flow: Measuring CSF Net Velocity in the Human Subarachnoid Space with 7T MRI. *bioRxiv* **2025**, *Preprint*. [CrossRef]
48. Eide, P.K.; Ringstad, G. Functional Analysis of the Human Perivascular Subarachnoid Space. *Nat. Commun.* **2024**, *15*, 2001. [CrossRef] [PubMed]
49. Sharp, M.K.; Carare, R.O.; Martin, B.A. Dispersion in porous media in oscillatory flow between flat plates: Applications to intrathecal, periarterial and paraarterial solute transport in the central nervous system. *Fluids Barriers CNS* **2019**, *16*, 13. [CrossRef]
50. Sereno, M.I.; Diedrichsen, J.; Tachrount, M.; Testa-Silva, G.; d'Arceuil, H.; DeZeeuw, C. The Human Cerebellum Has Almost 80% of the Surface Area of the Neocortex. *Proc. Natl. Acad. Sci. USA* **2020**, *117*, 19538–19543. [CrossRef] [PubMed]
51. Mestre, H.; Tithof, J.; Du, T.; Song, W.; Peng, W.; Sweeney, A.M.; Olveda, G.; Thomas, J.H.; Nedergaard, M.; Kelley, D.H. Flow of Cerebrospinal Fluid Is Driven by Arterial Pulsations and Is Reduced in Hypertension. *Nat. Commun.* **2018**, *9*, 4878. [CrossRef]
52. Raghunandan, A.; Ladron-de-Guevara, A.; Tithof, J.; Mestre, H.; Du, T.; Nedergaard, M.; Thomas, J.H.; Kelley, D.H. Bulk flow of cerebrospinal fluid observed in periarterial spaces is not an artifact of injection. *eLife* **2021**, *10*, e65958. [CrossRef]
53. Wright, A.M.; Wu, Y.-C.; Yang, H.-C.; Risacher, S.L.; Saykin, A.J.; Tong, Y.; Wen, Q. Coupled Pulsatile Vascular and Paravascular Fluid Dynamics in the Human Brain. *Fluids Barriers CNS* **2024**, *21*, 71. [CrossRef]
54. Wu, Y.; Xu, F.; Zhu, D.; Li, A.M.; Wang, K.; Qin, Q.; Xu, J. Cerebrospinal Fluid Flow within Ventricles and Subarachnoid Space Evaluated by Velocity Selective Spin Labeling MRI. *NeuroImage* **2025**, *309*, 121095. [CrossRef]
55. Ringstad, G.; Valnes, L.M.; Dale, A.M.; Pripp, A.H.; Vatnehol, S.A.S.; Emblem, K.E.; Mardal, K.A.; Eide, P.K. Brain-wide glymphatic enhancement and clearance in humans assessed with MRI. *JCI Insight* **2018**, *3*, e121537. [CrossRef]
56. Eide, P.K.; Vinje, V.; Pripp, A.H.; Mardal, K.-A.; Ringstad, G. Sleep deprivation impairs molecular clearance from the human brain. *Brain* **2021**, *144*, 863–874. [CrossRef]
57. Bojarskaite, L.; Vallet, A.; Bjørnstad, D.M.; Gullestad Binder, K.M.; Cunen, C.; Heuser, K.; Kuchta, M.; Mardal, K.A.; Enger, R. Sleep cycle-dependent vascular dynamics in male mice and the predicted effects on perivascular cerebrospinal fluid flow and solute transport. *Nat. Commun.* **2023**, *14*, 953. [CrossRef]
58. Gan, Y.; Holstein-Rønsbo, S.; Nedergaard, M.; Boster, K.A.S.; Thomas, J.H.; Kelley, D.H. Perivascular Pumping of Cerebrospinal Fluid in the Brain with a Valve Mechanism. *J. R. Soc. Interface* **2023**, *20*, 20230288. [CrossRef] [PubMed]
59. Kelley, D.H.; Thomas, J.H. Cerebrospinal fluid flow. *Annu. Rev. Fluid Mech.* **2023**, *55*, 237–264. [CrossRef] [PubMed]
60. Balédent, O.; Czosnyka, Z.; Czosnyka, M. "Bucket" cerebrospinal fluid bulk flow—Is it a fact or a fiction? *Acta Neurochir.* **2019**, *161*, 257–258. [CrossRef]
61. Min Rivas, F.; Liu, J.; Martell, B.C.; Du, T.; Mestre, H.; Nedergaard, M.; Tithof, J.; Thomas, J.H.; Kelley, D.H. Surface periarterial spaces of the mouse brain are open, not porous. *J. R. Soc. Interface* **2020**, *17*, 20200593. [CrossRef] [PubMed]